



Application of Scratch Testing for the Assessment of the Adherent Properties of Scales and CO₂ Corrosion Product Layers and their Relation to Corrosion

Claudia Prieto, Hamed Mansoori, Bruce Brown, Marc Singer, David Young*

Institute for Corrosion and Multiphase Technology, Department of Chemical and Biomolecular Engineering, Ohio University, United States

ARTICLE INFO

Keywords:

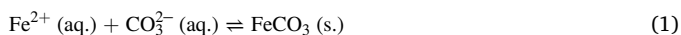
corrosion product layer
mechanical integrity
scratch test
calcium carbonate
iron carbonate

ABSTRACT

Protective corrosion product layers, such as iron carbonate, can govern pipeline corrosion; their formation being associated with operational conditions (high [Fe²⁺], pH > 6.0, T > 70 °C). Brines contain Ca²⁺ that can incorporate as a substitutional cation in the iron carbonate lattice, potentially compromising the mechanical integrity of the protective layer. This work utilized scratch testing as an analytical technique that provides more information on layer adherence than indentation methods. It was demonstrated that the presence of iron calcium carbonate layers contributes to the formation of a protective and mechanically stable iron carbonate layer adjacent to the steel surface.

1. Introduction

The main product due to corrosion of mild steel at pH values higher than 6.0 in the presence of CO₂ is iron carbonate (FeCO₃) [1]. The iron carbonate is formed through precipitation, by its heterogeneous nucleation and growth, on the metal surface [1]. The overall reaction is:



Sun [2] fully discusses the main parameters affecting the precipitation and formation of an iron carbonate layer, which is assumed to be governed by the solubility product (K_{sp}) and crystal growth rate [1,3]. Eq. (2) shows that the saturation value is a function of ferrous ion concentration (Fe²⁺) and carbonate ion concentration (CO₃²⁻).

$$S_{\text{FeCO}_3} = \frac{[\text{Fe}^{2+}][\text{CO}_3^{2-}]}{K_{sp}} \quad (2)$$

When the value of S determined by Eq. (2) is more significant than unity the resultant condition is termed as supersaturation, which is favorable for the formation of iron carbonate [2–4]. In the same manner, the presence of aqueous calcium ions (Ca²⁺) in transmission pipelines has the potential to lead to the formation of calcium carbonate (CaCO₃, also mineralogically known as calcite) in CO₂ corrosion environments [5]. These layers have been studied comprehensively in the framework of corrosion. According to Nescic and Lee [6], the formation of an iron

carbonate layer follows precipitation from a supersaturated solution and growth as a polycrystalline layer. More recently, Mansoori, et al., proposed a similar growth mechanism for calcium carbonate and iron calcium carbonate on steel [7]. Moreover, Rizzo, et al., proposed that the precipitation of the calcium carbonate results in a drop in the pH causing a change in the thermodynamic conditions that hinders the precipitation of iron carbonate [8].

These layers can confer protection against corrosion [5–7,9]. However, their protectiveness is dependent on their mechanical integrity [10–12]. A total or partial removal of these layers has been postulated to lead to localized corrosion [10–12]. Attending this problem, many studies have elucidated the removal of corrosion product layers via theoretical, mechanical, and chemical means. Matamoros-Veloza suggested that substitutional calcium in iron carbonate can create distortion in the geometrical structure of the carbonate, affecting the mechanical properties of the layer [13]. However, no direct measurements of such properties were reported. Ruzic, et al. [14–16], studied the mechanical, chemical, and chemo-mechanical removal of a protective iron carbonate layer with a rotating cylinder electrode at high rotational speeds of 7,000 and 10,000 rpm which confer calculated wall shear stress values of 45 and 82 Pa, respectively. The authors concluded that the mechanical failure induced by shear stress at high velocity of a rotating cylinder electrode can generate a partial delamination of a formed iron carbonate layer. However, as pointed out by Paolinelli and Carr [17], rotating

* Corresponding author.

E-mail address: youngd1@ohio.edu (D. Young).

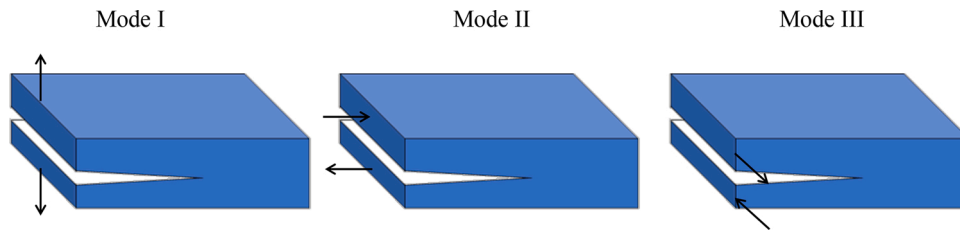


Fig. 1. Types of applied force to generate crack propagation: Mode I corresponds to tensile forces normal to the crack; Mode II corresponds to sliding forces (parallel to the crack); Mode III corresponds to the ‘tearing’ mode. The forces are parallel to the crack front. Adapted from Richard and Sander [23].

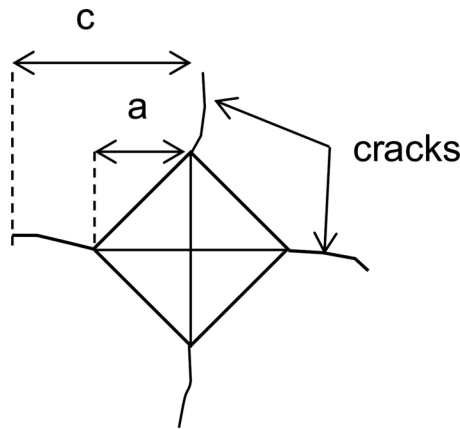


Fig. 2. Vickers indentation mark on a brittle material. Cracks generated during the test are related to the fracture toughness. Adapted from [22].

cylinder electrode systems might induce undesired stresses that affect the interpretation of results at high rotational speeds of cylindrical electrodes. Therefore, the mechanical removal of layers might come from a different phenomenon than wall shear stress. Consequently, results from rotating cylinder electrodes are potentially compromised. Some researchers have utilized the pull-off test to determine the adherence of iron carbonate layers [9,12]. However, there are some criticisms regarding the reliability of the pull-off test [18–20]. Factors such as type of glue, skill of the operator, and thickness of the layer might influence the result of the test [18–20]. Moreover, the test might not differentiate between adhesive (detachment of the layer from the substrate) or cohesive failure (break of the very same layer).

Another approach to establish the likelihood of detachment of a corrosion product layer/scale is the determination of the fracture toughness (K_{IC}) via Vickers nanoindentation [10–12,21]. Fracture toughness is the mechanical property of a material that indicates how facile a crack can propagate in the substance [22]. Depending on the force that generates the crack propagation, the fracture toughness can be divided into three modes as shown in Fig. 1.

For the case of brittle materials deposited on a metal substrate, Mode I (K_{IC}) is the most commonly reported mode of failure [10–12,21]. Given the similitudes to corrosion layers / scale deposition, the crack propagation of corrosion product layers and scales is assumed to depend on the level of residual tensile stresses in the layer [24]. The fracture toughness in the layer can be estimated with the following semi-empirical relationship:

$$K_{IC} = \alpha \left(\frac{E}{H_V} \right)^m \left(\frac{F_N}{c^n} \right) \quad (3)$$

Where K_{IC} is the fracture toughness, in $\text{MPa m}^{1/2}$; α , m , n are constants of proportionality, E is the Young’s modulus of the material, in Pa; H_V is the Vickers hardness of the material, in kg mm^{-2} , obtained from the parameter a in Fig. 2, and c is the crack length as shown in Fig. 2, in m or μm , depending on the constant of proportionality.

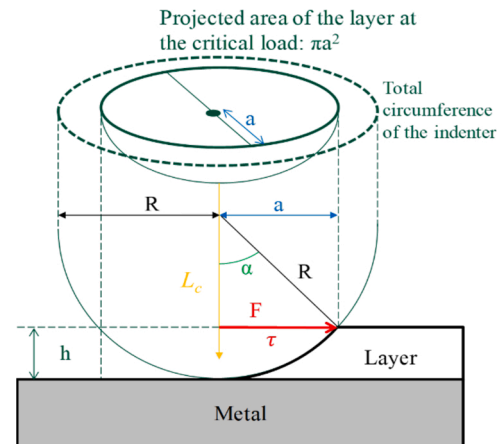


Fig. 3. The principle of scratching to remove a layer (white) from a metal substrate (gray). Related physical magnitudes are colored-related: L_c is the critical load (vertical load of the indenter when it reaches the substrate); F is the tangential force and τ the shear stress (red-colored vectors); R is the total radius of the indenter; a is the radius at the critical load (when the indenter reached the metal substrate); h is the thickness of the layer.

In the case of corrosion product layers, many researchers have suggested values of α from 0.016 to 0.04, and values of 0.5 and 1.5 for m and n , respectively [10–12,21]. Nonetheless, the Vickers indentation fracture (VIF) method has been precisely criticized for requiring different calibration constants to ‘match’ fracture toughness values obtained with other methods [25]. Certainly, there are more reliable methods to determine the fracture toughness of a material, such as chevron notch bar, double cantilever beam, and single-edge notched beam [11,26]. However, those tests require bulk specimens with a well-defined geometry, which result in impracticalities for the purposes of studying corrosion product layers/scales. For all the reasons mentioned, this effort proposes a complement of the VIF assessment of corrosion product layers with use of a well-known technique from tribology science: scratch testing. Scratch testing is a tribological technique widely utilized, among other applications, in the determination of adhesive forces between a substrate and thin layers [27–29]. This method is considered a robust technique to obtain information about the adhesion of a film to a substrate [28,30].

The scratch testing theory applicable to corrosion product layers is based on the work of Laugier, Perry, and Weaver [31–33]. Regarding the research reported herein, the Ollivier and Matthews mathematical model for hard thin films deposited on a flexible substrate was used to calculate the shear stress from the experimental forces [34]. The authors assumed that, at the critical load, the plastic deformation of the substrate is negligible for flexible substrates. There are also two implicit assumptions: internal stresses are negligible, and the scratch testing process is performed quasi-statically. In other words, the process occurs so slowly that the static analysis of the forces is valid. Consequently, the resulting tangential force is a linear function of the normal force, independent from the substrate. Such a tangential force is the sum of the

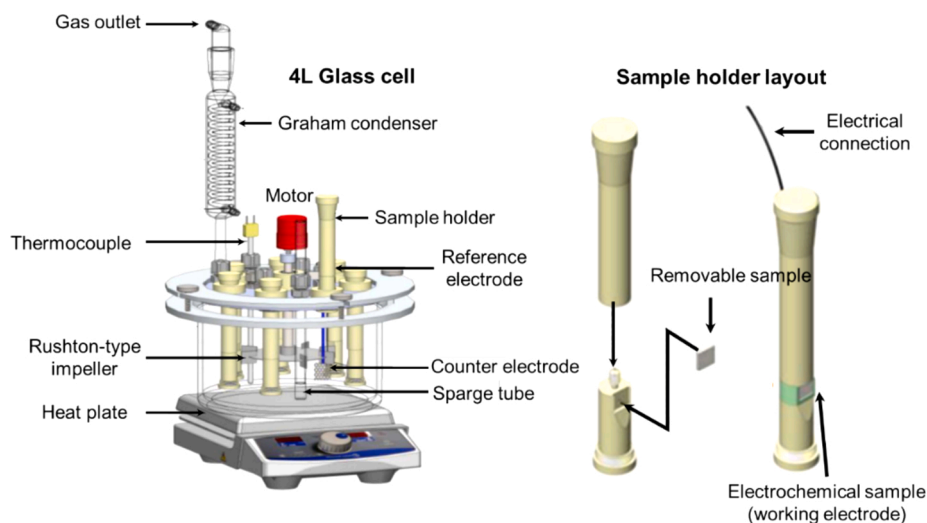


Fig. 4. Three electrode glass cell apparatus with impeller. Removable samples for scratch testing. Electrochemical sample for LPR measurements. Drawing courtesy of Cody Shafer, ICMT.

friction and ploughing term fully addressed by Bull, et al. [29]. Fig. 3 shows the geometrical parameters and forces involved in the determination of the tangential force to further transform it into shear stress.

The mathematical development of the formula is based upon the combination of geometrical parameters and the previously-mentioned forces, as discussed elsewhere [34]. This results in a formula that transforms the critical load into shear stress (τ) [34]:

$$\tau = \frac{L_c}{\pi a \sqrt{R^2 - a^2}} \quad (4)$$

Where: a is the radius of the projected area, in m; R is the indenter radius, in m, L_c is the critical load, in N, and τ is the shear stress, in Pa.

The research described herein utilizes Eq. (4) to comparatively assess the mechanical integrity of corrosion product layers and scales; specifically, iron carbonate, calcium carbonate and substitutional solid solutions of iron calcium carbonate. Results from the Vickers indentation fracture method are reported for comparative purposes. A larger propagation of the cracks in different corrosion product layers results in different K_{IC} values. This would imply that one material is more fragile than the other.

2. Experimental Method

2.1. Formation of Iron Carbonate Layers

To develop an iron carbonate layer, a 1018 steel (UNS G10180, C 0.18 wt.%, Cu 0.18 wt.%, Cr 0.12 wt.%, Mn 0.75 wt.%, balance Fe) was utilized as the substrate. Fig. 4 shows the experimental setup.

A setup equipped with a Rushton-type impeller, as reported elsewhere [35], was utilized. Sample preparation included sequential polishing with silicon carbide abrasive paper of 150, 400 and 600 grit. The samples were ultrasonicated for 5 minutes with isopropyl alcohol, dried with a heat gun, and immediately immersed in the working solution (4 L of 1 wt.% NaCl). For scratch testing, flat square specimens of an exposed area of 1.6 cm² were placed in the sample holder. For electrochemical measurements, a special holder with an electrical connection was used. Before the immersion step, the working solution was heated to 80 °C. While heating, the solution was deoxygenated for at least 1 hour with CO₂ as the sparging gas. The gas was continuously sparged throughout all the experiment ensuring continuous positive pressure. The partial pressure of CO₂ for this experiment is 0.53 bar since the experiments were conducted at atmospheric pressure and 80 °C, the water vapor partial pressure is 0.47 bar. The experimental setup included a Graham

Table 1

Experimental Conditions to Develop a Uniform Layer of Iron Carbonate (FeCO₃).

Parameter	Value
Temperature of solution	80 °C
Sparge gas	CO ₂
Substrate material	UNS G10180 Steel
Solution	1 wt.% NaCl, 50 ppm _w FeCl ₂ (initial)
Impeller rotation speed	20 rpm
Mass transfer conditions	Equivalent to 0.5 m/s in a 0.1 m ID pipe [7]
pH	6.6 ± 0.1
Duration	3 days

condenser at the exit of the glass cell to mitigate evaporation of the solution. When the system reached equilibrium, the pH was close to 6.3. The pH was adjusted before each experiment to 6.6 by injecting a deoxygenated solution of 0.1 M NaHCO₃ as needed. Immediately after immersing the samples, a solution of FeCl₂ deoxygenated with nitrogen was injected to achieve 50 ppm_w of Fe²⁺; the iron carbonate saturation level value for the abovementioned conditions, as calculated with Eq. (2), is 45. The impeller rotation was set to 20 rpm. The mass transfer coefficient for this impeller was characterized in a previous research work [7]. The conditions are equivalent to a superficial water velocity of 0.5 m/s in a 0.1 m ID pipe. Table 1 shows the experimental conditions to develop such a uniform corrosion product layer.

2.2. Formation of Calcium Carbonate Layers

Calcium carbonate layers were formed in the same setup as for iron carbonate. In order to obtain a pure calcium carbonate scale on the metal substrate, a special procedure proposed by Mansoori, et al., [5] was followed: prepare a CO₂-sparged solution with 1 wt.% NaCl at 80 °C, set to a pH 6.2 with the addition of a solution of NaHCO₃, akin to the procedure described for iron carbonate. However, even though calcium carbonate exhibits a higher precipitation rate than iron carbonate, there exists the possibility of iron carbonate formation if sufficient ferrous ions are produced due to the natural corrosion of specimens. Therefore, the steel specimens were cathodically protected to avoid corrosion by polarizing the specimen throughout the experiment. To avoid an excessive production of gaseous hydrogen coming from the surface of the specimen that might hinder the precipitation of calcium carbonate, the cathodic protection was controlled by fixing the potential to -850 mV vs. a Ag/AgCl KCl saturated reference electrode. This potential was determined from experimental potentiodynamic polarization curves.

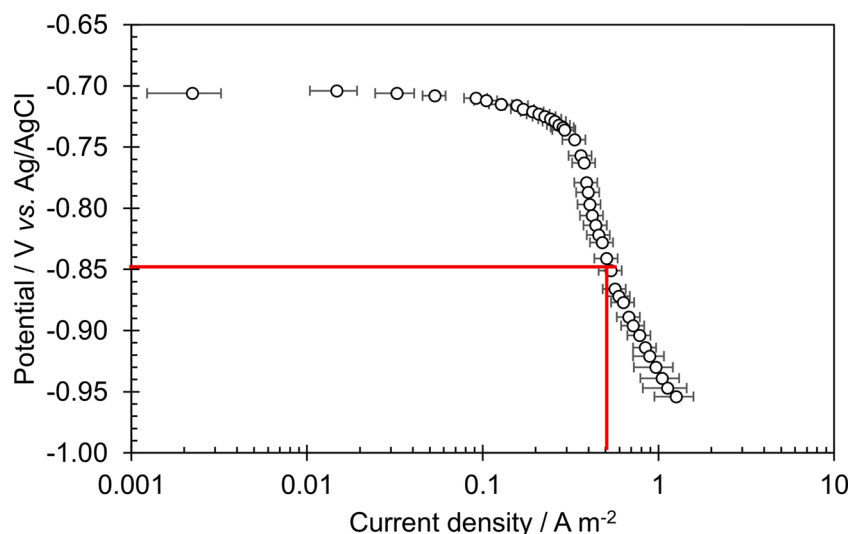


Fig. 5. Potentiodynamic polarization to determine the operating potential to cathodically protect the steel sample. (Error bars: maximum and minimum current at selected potentials from three independent experiments. Red lines: selected potential to cathodically protect the specimen.)

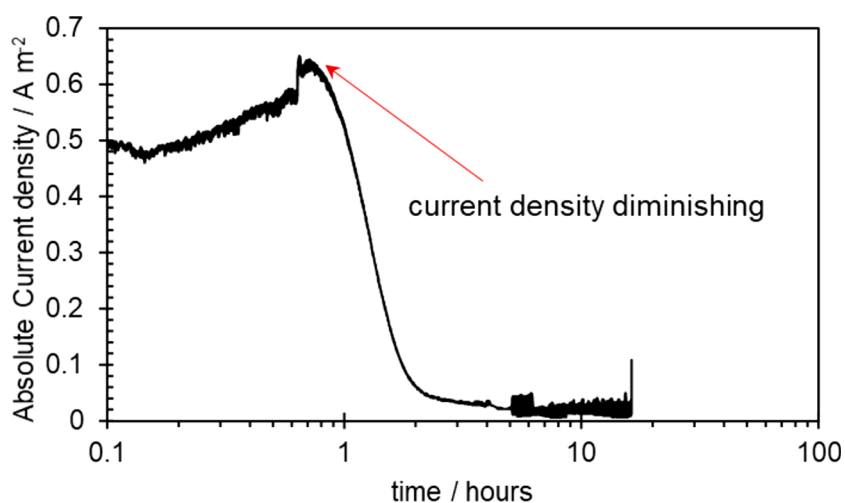


Fig. 6. Measured current at a fixed potential (-850 mV vs. Ag/AgCl). After the injection of 1000 ppm of Ca^{2+} in the form of CaCl_2 at the beginning of the experiment, the absolute current density diminished after *ca.* 1 hour. After 5 hours, the current remained virtually zero.

Table 2
Experimental Conditions to Develop a Calcium Carbonate Layer

Parameter	Value
Temperature of solution	80 °C
Sparge gas	CO_2
Substrate material	UNS G10180 Steel
Solution	1 wt.% NaCl + 400 ppm _w Ca^{2+}
pH	6.2 ± 0.1
Impeller rotation speed	20 rpm
Mass transfer conditions	Equivalent to 0.5 m/s in a 0.1 m ID pipe [7]
Duration	1 day (when the current density at a fixed potential reached virtually zero)

The goal was to find a balance between protecting the metal *via* cathodic protection and avoiding an excessive rate of hydrogen evolution. Three cathodic potentiodynamic polarization sweeps were run at a scan rate of 0.1 mV/s from the open circuit potential (OCP) up to -250 mV with respect to the OCP, as shown in Fig. 5.

The potential of -850 mV vs. Ag/AgCl KCl saturated was chosen since it was the lowest potential at which hydrogen bubbles were not visually detected. Lower potentials reach the water line for its reduction [36] and hydrogen bubbles are more evident. With the value chosen, after the sample is immersed and the cathodic protection is applied with the potentiostat, 400 ppm of calcium ions (Ca^{2+}) in the form of calcium chloride (CaCl_2) were injected to promote supersaturation of calcium carbonate (CaCO_3). As shown by Fig. 6, the current density is monitored to observe the precipitation of calcium carbonate. Current reaching almost zero indicates the precipitation of a calcium carbonate layer since the scale blocks the surface and hinders the associated Faradaic current densities. pH was controlled by the injection of a deoxygenated NaHCO_3 solution as needed (Table 2).

2.3. Formation of an iron calcium carbonate layer ($\text{Fe}_x\text{Ca}_{(1-x)}\text{CO}_3$)

Carbonates from the mineralogy perspective are solid phases with a cation and a triangular carbonate group (CO_3^{2-}) [37]. They can co-precipitate from aqueous solutions with isomorphic substitution of divalent cations in their crystal lattices [37]. Such a co-precipitation readily leads to a substitutional solid solution according to the overall

Table 3

Experimental conditions to develop an iron carbonate layer with substitutional calcium.

Parameter	Value
Temperature of solution	80 °C
Spurge gas	CO ₂
Substrate material	UNS G10180
Solution	1 wt.% NaCl + Ca(OH) ₂ as needed
pH	Initially 10.5, then 6.2 ± 0.1
Impeller rotation speed	20 rpm
Mass transfer conditions	Equivalent to 0.5 m/s in a 0.1 m ID pipe [7]
Duration	1, 2, 4, and 7 days

expression:



For this study, the substitutional cation is the ferrous ion (Fe²⁺) since the precipitation of calcium carbonate is relatively faster than the iron calcium carbonate solid solution [37,38] and an initial precipitation of calcium carbonate is expected before onset of solid solution precipitation. Rizzo, et al., studied the influence of CaCO₃ precipitation on the stability of FeCO₃ in terms of protectiveness and morphology. The authors concluded that the precipitation of calcium carbonate led to the drop in pH and a change in the saturation conditions of iron carbonate that hindered its precipitation [8]. Moreover, this condition leads to the dissolution of iron carbonate. To avoid any influence of the pH drop and supersaturate with calcium ions the working solution, a solution of calcium hydroxide, Ca(OH)₂, was injected until a pH of 10.5 was achieved. As the surface layer precipitated, the pH dropped back gradually to its target value of 6.2. The pH was maintained at this point with the injection of a solution of NaHCO₃ as needed. Since corrosion of the steel substrate was also occurring during this experiment, high content of ferrous ions was also expected, conducive to the formation of FeCO₃. The experiment was performed over different numbers of days to have a variation in the degree of substitutional iron in the formed layers. Table 3 summarizes the conditions at which the experiments were conducted.

2.4. Electrochemical corrosion rate measurements

As illustrated by Fig. 4, a three-electrode glass cell was utilized to determine the corrosion rates by obtaining the charge transfer resistance using linear polarization resistance (LPR) as per ASTM G102 [39]. The corrosion currents (I_{corr} in A) were obtained by subtracting the solution resistance (R_S in Ohm) to the polarization resistance (R_p in Ohm) to obtain the charge transfer resistance (R_{CT} in Ohm) and with a Stern-Geary equation with a Stern-Geary constant (B) of 26 mV for the case of CO₂ corrosion:

$$I_{corr} = \frac{B}{R_p - R_S} = \frac{B}{R_{CT}} \quad (6)$$

It must be mentioned that the Stern-Geary constant of $B = 26$ mV was selected from work performed by other researchers that utilized best fit comparison between current densities and weight loss corrosion measurements. The conditions tested might drift during the test. However, the position of this research was to use a reasonable value of B and keep it constant for the testing conditions as proposed by Mansoori, et al. [7]. Corrosion current densities were then converted into corrosion rates in mm/y using Faraday's law [40]:

$$W = \frac{M}{nF} I_{corr} t \quad (7)$$

Where t is the time of corrosion (s), M_W is the molar mass of the metal (55.8 g/mol for iron), F is Faraday's constant (96 485 C mol⁻¹); n is the number of electrons transferred per mole of metal. In the case of iron

Table 4

Scratch test conditions to determine the critical load of all the specimens tested.

Parameter	Value
Type of load	Progressive
Initial load (N)	0.01
Final load (N)	0.8
Loading rate (N/min)	0.8
Scratch length (mm)	3
Scratching speed (mm/min)	3
Test duration	1 minute
Indenter geometry	120° Cone

dissolution $n = 2$, as shown in the following anodic reaction:



Eq. (7) can be used to calculate the corrosion rate with some transformations. Starting by using the density $\rho = W/V$, the volume lost due to corrosion and to obtain the corrosion rate in linear penetration (CR), the volume is divided by the area exposed to the metal and by units of time:

$$\text{CR} = \frac{M}{\rho n F A} I_{corr} = \text{CR} = \frac{M}{\rho n F} i_{corr} \quad (9)$$

where i_{corr} is current density (A/cm²) obtained from the product of the total current (I_{corr}) and the cross-sectional area (A). Finally, for the case of iron, $\rho = 7.87$ g/cm³ and transforming corrosion current density from A/cm² into A/m², and converting corrosion rate from cm/s to mm/year:

$$\text{CR} \left(\frac{\text{mm}}{\text{year}} \right) = (1.158) i_{corr} \quad (10)$$

For the cathodically protected specimens, the LPR data was taken at OCP by temporarily stopping the polarization (*i.e.*, the protection). The LPR measurements were taken after the open potential had stabilized at the OCP, this typically took a few minutes. After the measurement, cathodic polarization was resumed.

2.5. Optical and Chemical Characterization of Corrosion Products

Scanning electron microscopy (SEM) and energy dispersive X-ray spectroscopy (EDS), in conjunction with X-ray diffraction (XRD), was used to determine the extent of steel coverage and composition of corrosion products. A Rigaku UltimaIV X-ray diffractometer (monochromatic CuK α radiation, $\lambda = 0.15405$ nm) at a scan rate of 2° min⁻¹ was used. Other researchers have successfully applied these techniques to characterize corrosion product layers [41,42]. The results for the X-ray diffraction patterns of the layers presented in the research reported herein that confirms the presence of Fe_xCa_yCO₃ layers have been published elsewhere [35].

2.6. Procedure to Determine the Adhesion Forces and Critical Shear Stress via Scratch Testing

In order to determine the critical shear stress for iron carbonate removal, this research followed the methodology described by Bull, et al. [43], and the mathematical model from Ollivier and Matthews [34]:

- 1 Determine the hardness of the layer and the substrate to have a qualitative understanding of the mode of failure of the layer by using the qualitative failure map reported by Bull, et al. [43].
- 2 Estimate the critical load force from the progressive load scratch test.
- 3 By using the constant load scratch test, corroborate the previously estimated critical load.

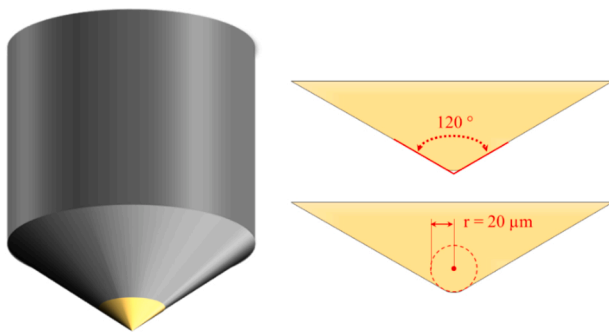


Fig. 7. Sketch of the indenter utilized for scratch testing. Angle of the tip is 120° and the radius $20\ \mu\text{m}$.

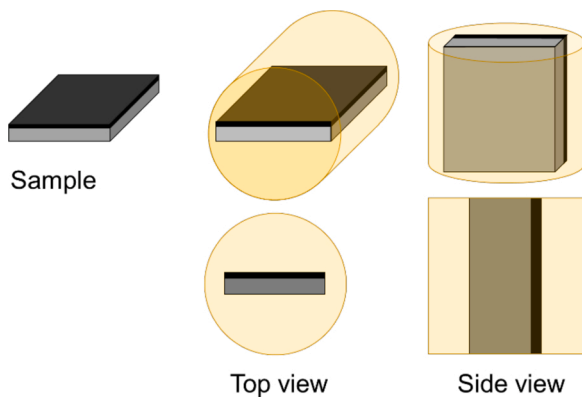


Fig. 8. Sample preparation for side fracture toughness determination. The samples were mounted in epoxy and ground/polished until both sides of the specimen were flush and parallel to the epoxy.

- Utilize the proposed mathematical model to transform the critical load into the corresponding shear stress by using Eq. (4).

The conditions for the scratch test are given by

Table 4 and the geometry specifications of the indenter is given by Fig. 7. It must be noted that the scratch speed was set to a low value of $3\ \text{mm/min}$ due to the implicit assumption of the mathematical model of quasistatic conditions.

2.7. Fracture toughness

At first glance it seems odd to use Vickers indentation fracture toughness determinations for corrosion product layers. However, these results are intended to be used to establish tendencies/trends and not for absolute values of fracture toughness of the layer. These results will be compared to those obtained in the scratch test to find a correlation between both techniques. Another point to consider is that fracture toughness is dependent on the residual tensile stresses on thin layers [44]. Therefore, the distribution of such stresses might produce anisotropy in the corrosion product layers. For example, the cross-section fracture toughness would not be the same as the fracture toughness from the top. Consequently, this study explored the fracture toughness in the cross-section of the corrosion product layers. For the case of cross-section testing, the specimens were mounted in epoxy and cut in cross-section as shown by Fig. 8. Next, the specimens were ground with 180 grit abrasive paper until both sides of the steel specimen are flush to the surface. In this way, an effect of resin cushioning during the indentation can be avoided since the steel is a stiffer material than the epoxy. Care was taken to maintain a parallel plane between the two faces.

For the cross-section testing side only, the samples were sequentially

Table 5
Scratch test conditions to determine the critical load of all the specimens tested.

Parameter	Value
Maximum force	2, 20 mN
Loading rate	4, 40 mN/min
Unloading rate	4, 40 mN/min
Computation method	ASTM E2546-15
Indenter type	Vickers

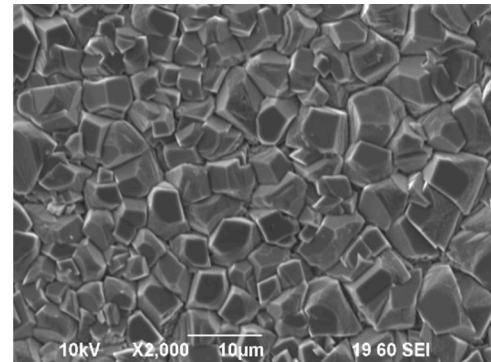


Fig. 9. Iron carbonate layer formed.

ground with 150, 400, and 600 grit abrasive paper. For both top and cross-section testing, the specimens were sequentially polished with 9, 3, and $0.25\ \mu\text{m}$ oil-based diamond suspension with a polishing cloth. The samples were sonicated with isopropyl alcohol and carefully dried with cold nitrogen gas. Vickers nanoindentation tests were performed with a Nanovea NH161115-1 Mechanical Tester at 20 mN loading force (2 mN for iron carbonate in the cross-section). The measurement parameters are given in Table 5.

To calculate the fracture toughness (K_{IC}), optical microscopy was used to measure the crack length and the diagonals from the Vickers' indenter print as shown in Fig. 2. Eq. (1) was used to calculate the fracture toughness range with α values of 0.016 and 0.04, and values of 0.5 and 1.5 for m and n , respectively. The idea is to obtain a range of values of the fracture toughness for comparative purposes and not a single value.

3. Results and Discussion

3.1. Surface Characterization

3.1.1. Iron Carbonate

Fig. 9 shows an SEM image of the developed iron carbonate layer. The thickness and the chemical signature of iron carbonate were determined by cross-section analysis and EDS, respectively (Fig. 10).

The XRD pattern of the specimen confirmed the presence of iron carbonate, as shown in Fig. 11.

3.1.2. Calcium Carbonate

The pure calcium carbonate was characterized via SEM, as shown in Fig. 12. Cross-section analysis showed that the average thickness of the layer is $18.5\ \mu\text{m}$. Fig. 12 also shows that the layer is compositionally homogeneous (via EDS mapping analysis), corresponding to calcium carbonate.

Fig. 13 shows the XRD pattern of the scale and its comparison with a literature pattern of calcite (CaCO_3).

3.1.3. Iron Calcium Carbonate

SEM images (Figs. 14 and 15) show the morphology of the iron/calcium carbonate ($\text{Fe}_x\text{Ca}_y\text{CO}_3$; $x + y = 1$) layers through different days.

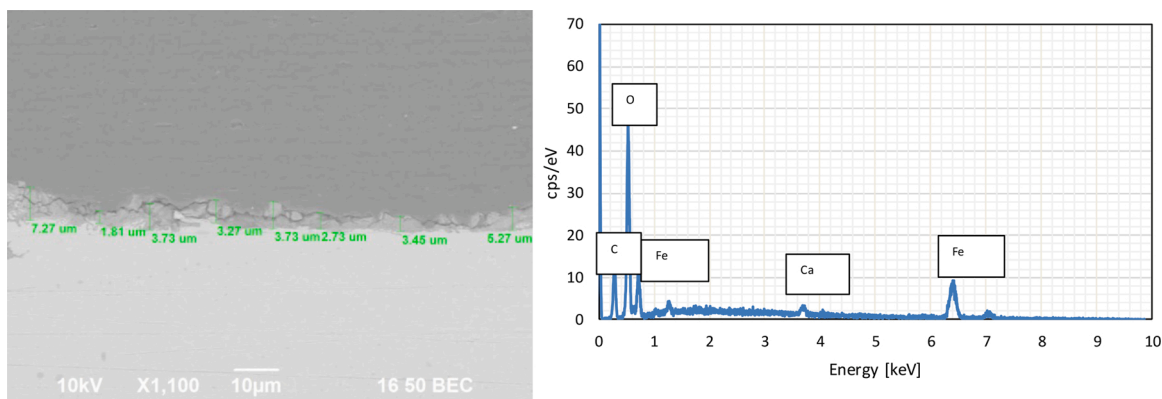


Fig. 10. The cross-section area of the iron carbonate layer. EDS data supported the formation of iron carbonate.

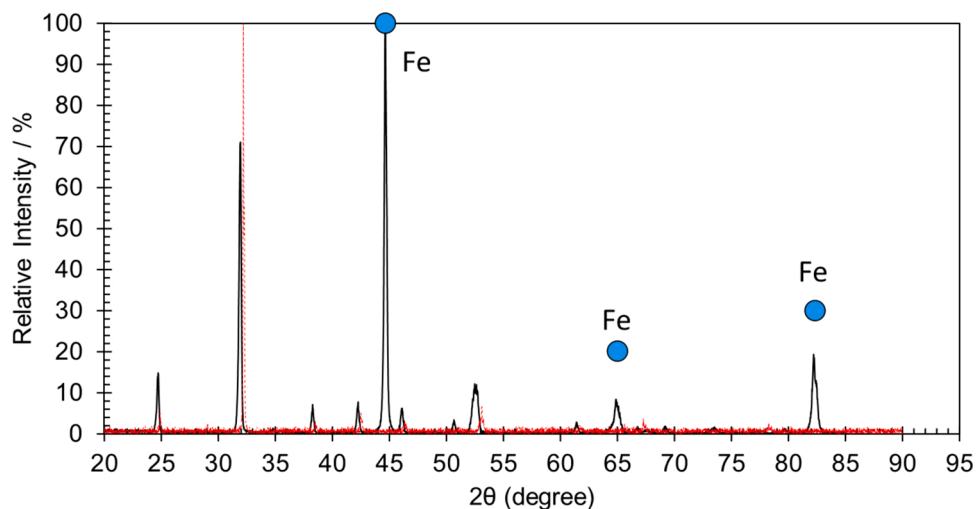


Fig. 11. XRD pattern of the generated corrosion product layer (black) compared with the pattern of siderite, FeCO₃, (red) [45]. The most prominent peaks (marked with blue circles) correspond to XRD iron peaks [45].

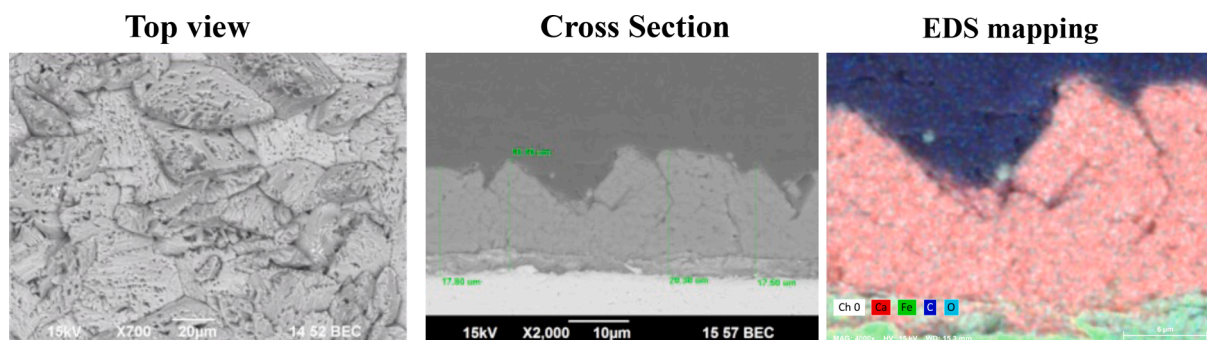


Fig. 12. Top view and cross-section analysis of a pure calcium carbonate layer. The thickness was determined to be 18.5 ± 1.3 μm. Right figure: EDS mapping cross-section analysis of the calcium carbonate layer formed as a scale.

The average thickness of the scale increased up to 25 μm. EDS analysis, shown in Fig. 15, revealed that at the first stages (day 1) the calcium carbonate is dominant. However, an iron carbonate layer underneath the first layer of calcium carbonate is formed. In the following section, the effect of the change in the composition of the layer on mechanical properties will be shown.

3.1.4. Fe_xCa_yCO₃ XRD Data Processing

As stated above, the results for the X-ray diffraction patterns of the layers presented in the research reported herein that confirms the

presence of Fe_xCa_yCO₃ layers have been published elsewhere [35]. Using such data, the determination of the molar fraction composition of substitutional Ca into the lattice of the iron calcium carbonate layers was performed by a method described by Hua, et al., [46]. Firstly, d-space of an hexagonal lattice structure can be expressed by Eq. (11) [47]:

$$\frac{1}{d^2} = \frac{4}{3} \left(\frac{h^2 + hk + k^2}{a^2} \right) + \frac{l^2}{c^2} \tag{11}$$

Where *h*, *k*, and *l* are the Miller indices corresponding to lattice

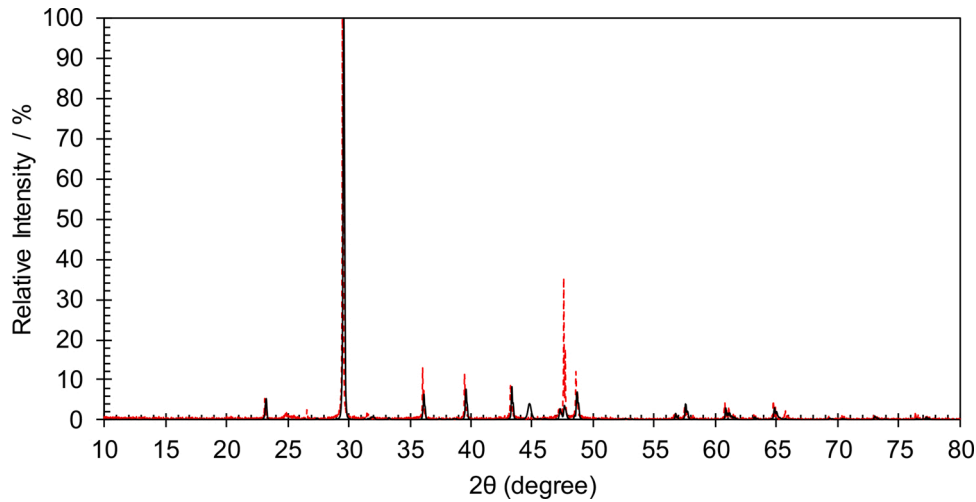


Fig. 13. XRD pattern of the generated scale (black) compared with the pattern of calcite, CaCO₃, (red) [45].

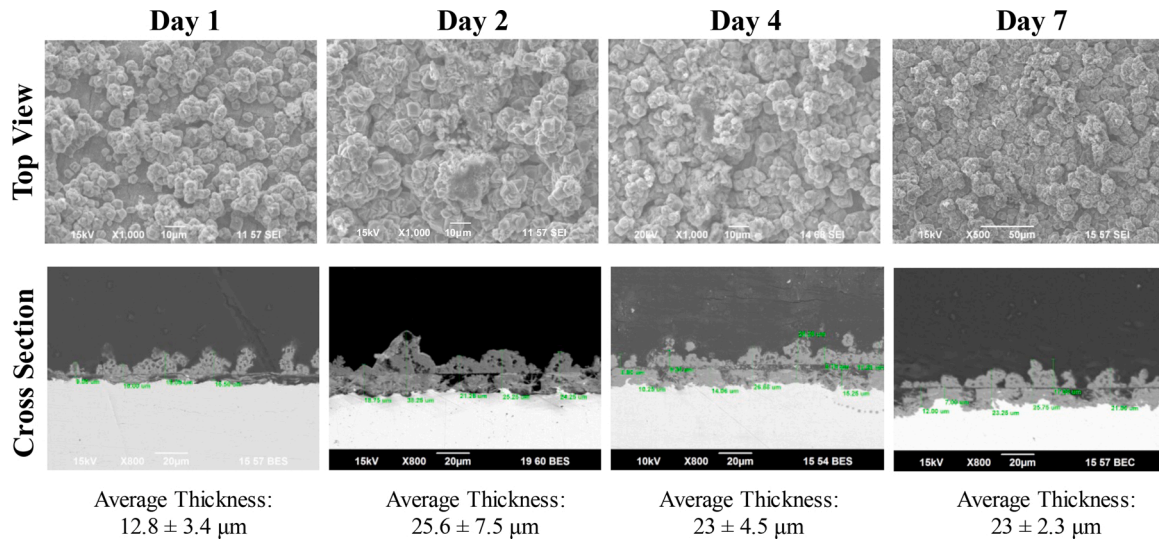


Fig. 14. Top view and cross-section analysis of the iron/calcium carbonate layers developed after different times (days). The thickness of the layer increased up to 25 μm.

planes [97] and parameter ‘d’ corresponds to the d-spacing calculated from Bragg’s law:

$$d = \frac{n\lambda}{2\sin\theta} \quad (12)$$

The parameters *c* and *a* are related through the unit cell volume (*V*) for a hexagonal lattice as shown by Eq. (13) [47]:

$$V = \frac{\sqrt{3}a^2c}{2} \quad (13)$$

Solving for *a*, Eq. (14) is obtained:

$$a = \sqrt{\frac{2V}{\sqrt{3}c}} \quad (14)$$

Finally, under the assumption that the unit cell volume and unit cell parameter *c* of calcite and siderite changes linearly with the change of the molar concentration of Ca²⁺ substituted into the lattice, it is possible to determine the average molar composition of the solid solution Fe_xCa_yCO₃. The change in parameter *c* and unit cell volume *V* are determined with Eq. (15) and (16) [46]:

$$c = 1.6885y + 15.373 \quad (15)$$

$$V = 74.107y + 291.34 \quad (16)$$

Therefore, based on the peak shifts for FeCO₃ located at the (104) inter-planar d-spacing, it is possible to determine the mole fraction of Ca in the Fe_xCa_yCO₃ solid state solution. The results are summarized in Table 6.

3.2. Mechanical Tests

3.2.1. Scratch Testing

3.2.1.1. Mode of Failure. The mode of failure is important because it gives information about how a failure propagates in layers [48]; whereas some propagate easily, other layers exhibit a lesser degree of failure propagation. The ASTM C1624 standard [48] distinguishes different types of failure: an initial critical load (L_C) associated with a damage on the layer by the indenter (partial removal of external material without causing cracks or spallation); the other is the adhesive failure in which there are some cracks generated by the tensile/compressive forces

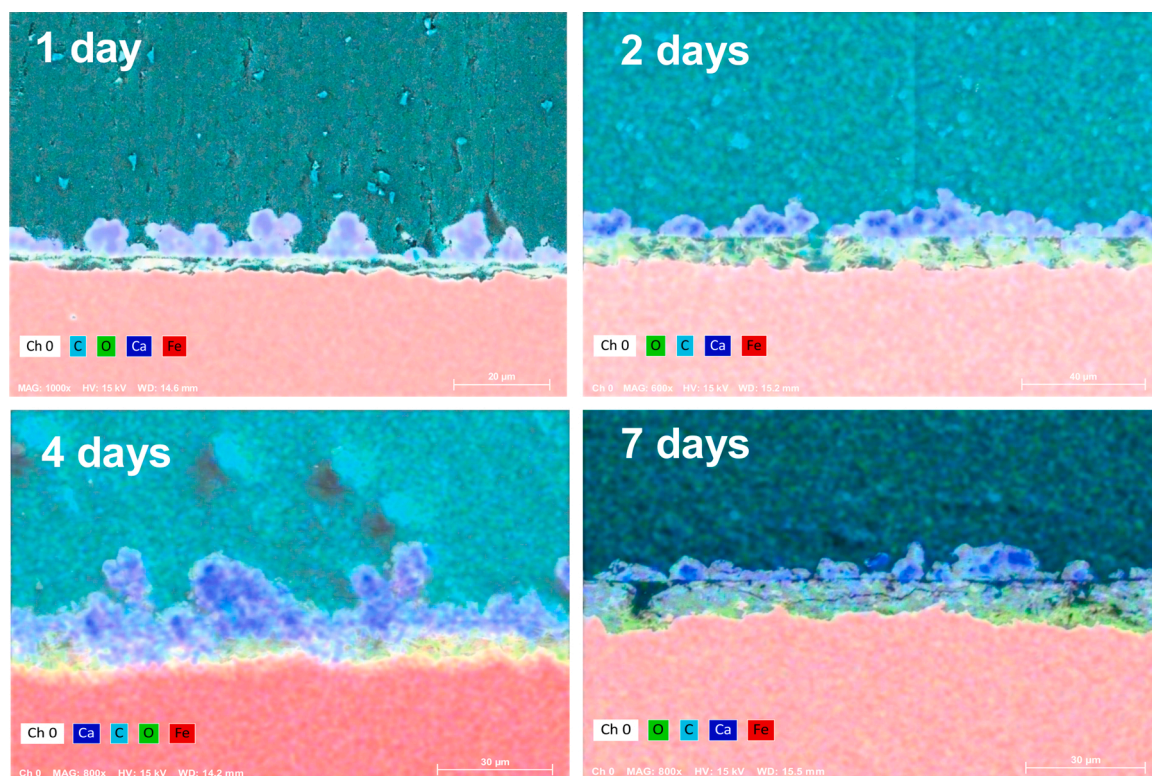


Fig. 15. EDS mapping analysis of the cross section of the iron/calcium carbonate layer developed after different times (days).

Table 6

Values for the mole fraction in the $Fe_xCa_yCO_3$ substitutional solids solutions.

Sample	x	y
1 day	0.56	0.44
2 days	0.61	0.39
4 days	0.72	0.28
7 days	0.88	0.12

within the thin layer and some detachment of the layer without reaching the substrate. The critical failure associated with adhesive failure is the minimal loading force at which the scratch indenter removed the layer from the substrate (partially leaving some of the layer attached to the substrate). Finally, the total delamination is the point where the layer is removed from the substrate completely and continuously. These failures are typically detected by visual inspection. However, this work employed the use of backscatter imaging and EDS mapping to corroborate the exposure of the metal during adhesive failure.

Fig. 16 shows a comparison between the way the studied carbonate layers behave when the critical load is reached in the progressive load scratch test for each layer. According to the scratch atlas from ASTM

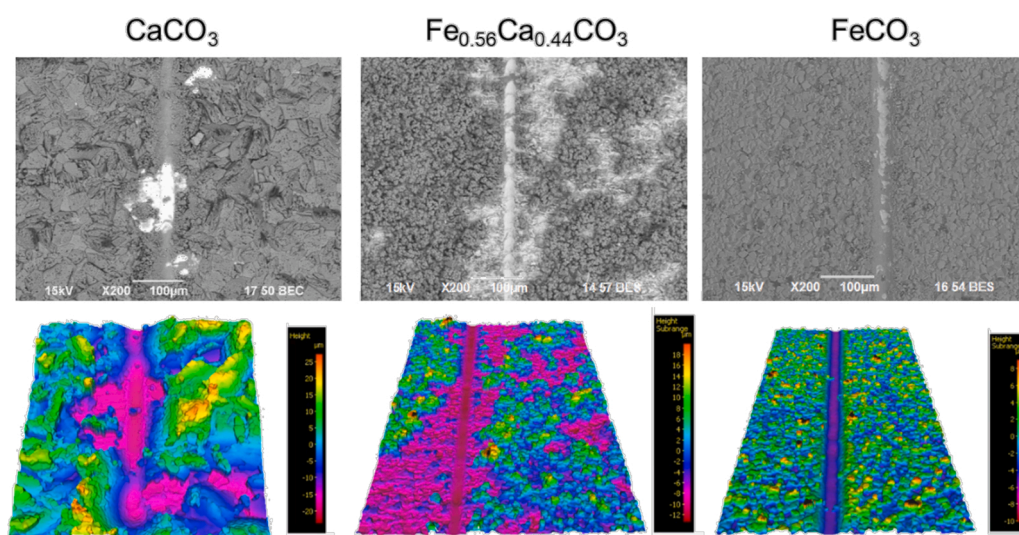


Fig. 16. Mode of failure for different types of scales and corrosion product layers. Top figures: backscatter images of the layers when the substrate was reached by the indenter. Bottom figures: corresponding profilometry data.



Fig. 17. Left-hand-side: Backscatter image of the critical load detected for iron carbonate at 250 mN of normal force. Bright zones are associated with the exposure of the metal substrate and corroborated with EDS mapping analysis (right-hand-side). Scratch direction: from bottom to top.

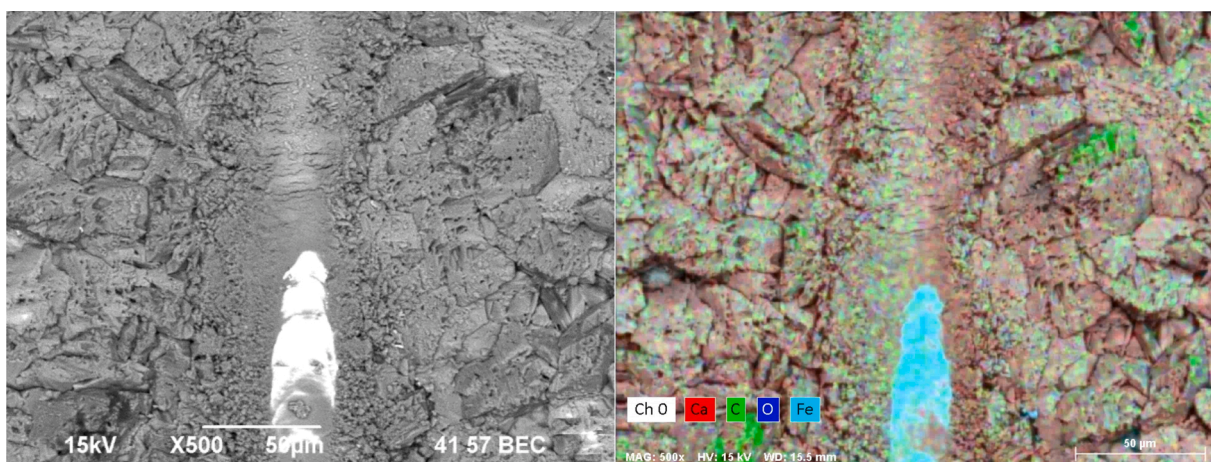


Fig. 18. Adhesive failure of calcium carbonate at 700 mN of normal force. Bright zones are associated with the exposure of the metal substrate and corroborated with EDS analysis. The iron substrate (in blue) was predominant in the scratch track at the failure. Scratch direction: from bottom to top.

C1624 [48], the mode of failure of the pure iron carbonate can be associated with buckling. This type of failure is usually attributed to highly adhesive layers that only fail in the zone where forces are exerted [48]. On the other hand, pure calcium carbonate and the iron calcium carbonate can be visually related to gross spallation. Such a failure is usually attributed to layers that exhibit low cohesive strength or high residual stresses [48]. One possible explanation can be the presence of calcium carbonate either decreases the adhesion strength of the iron carbonate layer due to an increase in porosity and a lower contact point between the layer and the substrate [13], or there are more residual stresses induced by the presence of iron as a substitutional element in the calcium carbonate layer since the replacement of the Fe^{2+} cation by a larger Ca^{2+} cation distorts the rhombohedral geometry of FeCO_3 , as postulated by Matamoros-Veloza, et al. [13].

3.2.1.2. Iron Carbonate. Progressive load scratch testing was utilized to determine the critical load of the layer. Fig. 17 shows the critical point at which the indenter reached the substrate corroborated by backscatter microscopy imaging and EDS mapping analysis. It is observed that there were some cracks at the bottom of the layer. According to Bull [43], they can be regarded as buckling cracks generated by sites of possible shear damage during the buckling mechanism; evidence of high adhesion forces between the iron carbonate and the iron and cohesion within the iron carbonate layer (no wedging or gross spallation before reaching the critical load). The associated shear stress value for this layer is 630 MPa.

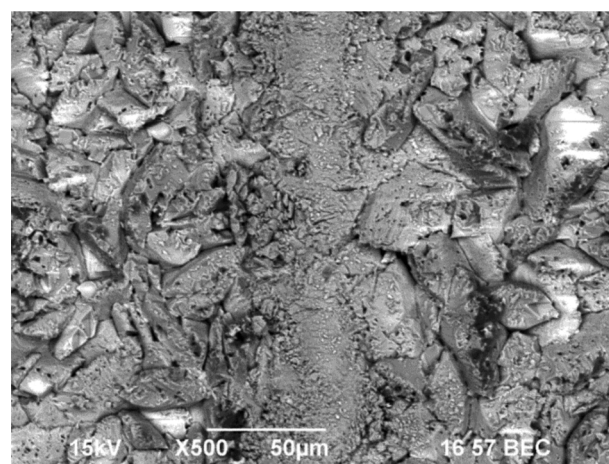


Fig. 19. 0.1 mN constant load. Cohesive failure detected. Scratch direction: from bottom to top.

3.2.1.3. Calcium Carbonate. Progressive load scratch tests from 0.1 mN to 800 mN were performed to determine the cohesive and adhesive failure of the calcium carbonate layer. Regarding the adhesive failure, the critical load was determined at 700 mN of normal force with an

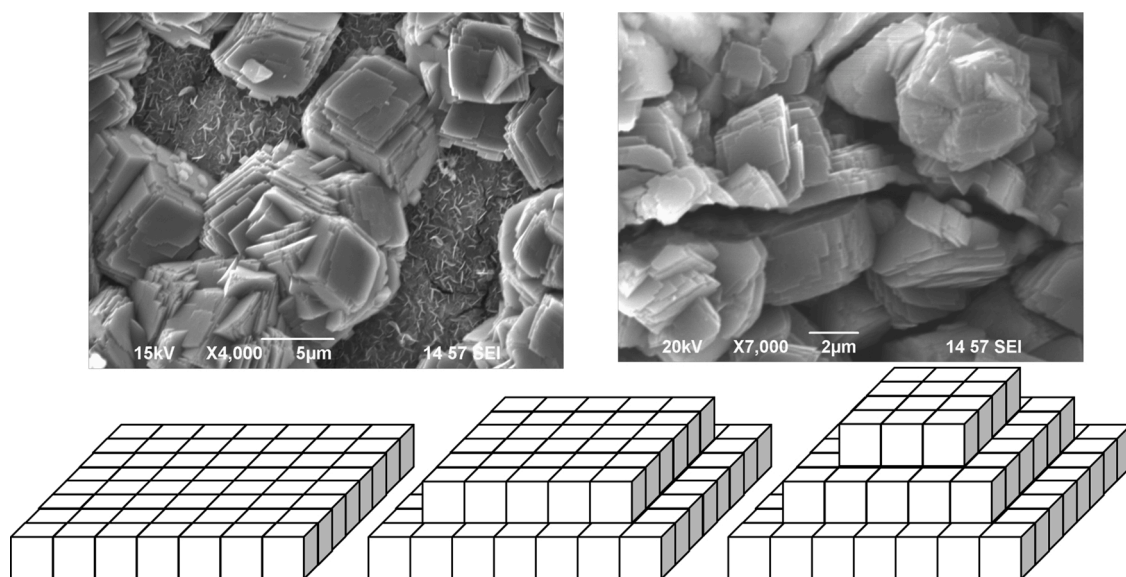


Fig. 20. Growing calcium carbonate crystals in a layer-by-layer fashion similar to the 'wedding cake' growth mechanism.

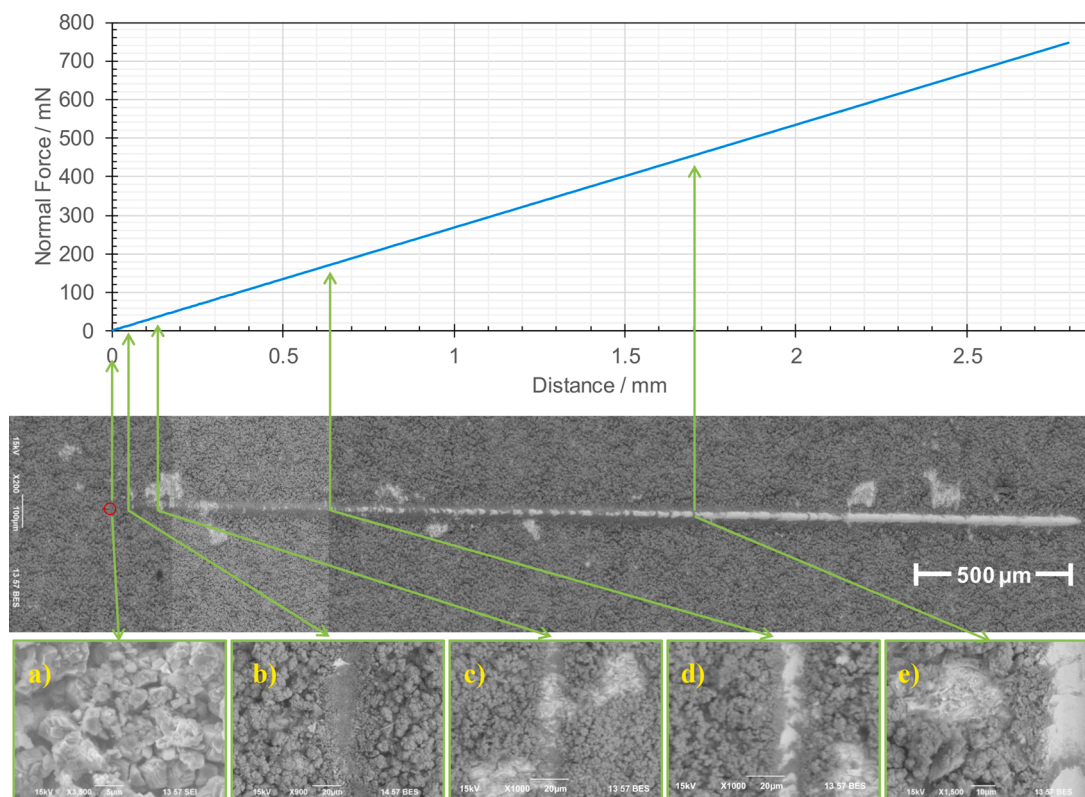


Fig. 21. Progressive load scratch test on a $\text{Fe}_{0.56}\text{Ca}_{0.44}\text{CO}_3$ layer. Red circle: contact point of the scratch tester. Each arrow indicates the load and the zoomed image of the damage. Zoomed images: a) contact point of the scratch tester tip; b) cohesive failure; c) adhesive failure (first detachment); d) adhesive failure (continuous detachment); e) total removal of the layer. Scratch direction: from left to right.

associated shear stress value of 1.2 ± 0.2 GPa; a value that almost doubles the critical shear stress for adhesive failure in the case of iron carbonate (630 MPa) [49].

Fig. 18 shows the SEM image in backscatter mode of the calcium carbonate failure and an EDS map.

However, in contrast to iron carbonate, it is noteworthy that even at 0.1 mN cohesive failure was detected; the outer part of the scale was pulverized by this force. Fig. 19 shows the cohesive failure detected,

with an associated shear stress of 160 kPa.

A possible explanation for this phenomenon is the epitaxial growth in the outer part of the layer. Fig. 20 shows a high-magnification SEM image of the outer crystals of the calcium carbonate layers. They show a 'wedding cake' type of morphology. Wedding cake growth [50] is a phenomenon in which the mechanism of crystal growth is through an epitaxial layer-by-layer mode before the coalescence of the crystals happens, as shown by Fig. 20. It has been reported that coherent and

Table 7
Failures Detected in the Progressive Load Scratch Test

Failure mode	Critical Load
Minimal force to produce damage	< 0.1 mN
Cohesive failure (groove formation, no cracks detected)	12.2 ± 2 mN
Adhesive failure (first detachment)	36.5 ± 1.5 mN
Adhesive failure (continuous detachment)	172 ± 15 mN
Total removal	425 ± 25 mN

layer-by-layer precipitated thin layers exhibit a high hardness and high brittleness [51]. In the context of scratch testing as postulated by Floro [52], these structural types, before coalescence, exhibit internal stresses that might lead to a detachment event. Strain induced instability can also explain the susceptibility to detachment of these structures [53,54], since a layer-by-layer grown crystal is susceptible to strain by external forces when a critical thickness is reached if coalescence has not happened.

3.2.1.4. Iron Calcium Carbonate. A progressive load scratch test was performed on the 1-day specimen to determine forces required for cohesive and adhesive failure. The 1-day specimen was chosen as it was considered to be a good representation of a solid solution intermediate between pure iron carbonate and pure calcium carbonate; the mole fractions of calcium and iron are approximately equal, as shown in the XRD analysis section, with the formula $\text{Fe}_{0.56}\text{Ca}_{0.44}\text{CO}_3$. Fig. 21 shows the SEM images of the layer after the scratch test. The results indicated that the contact force of the apparatus, in the order of 0.1 mN, caused damage to the layer; the crystals were shattered, as shown by Fig. 21a. As seen in Fig. 21b, a groove was detected when the force reached ca. 12 mN. This value was related to the cohesive failure of the layer since there were no cracks detected. Continuing with the progressive increase in the loading force, at values close to 37 mN, the first detachment of the layer was detected, as shown by Fig. 21c. Gross spallation of the adjacent scratch track resulted because of such failure. Fig. 21d shows a continuous detachment of the layer, which was detected at values close to 170

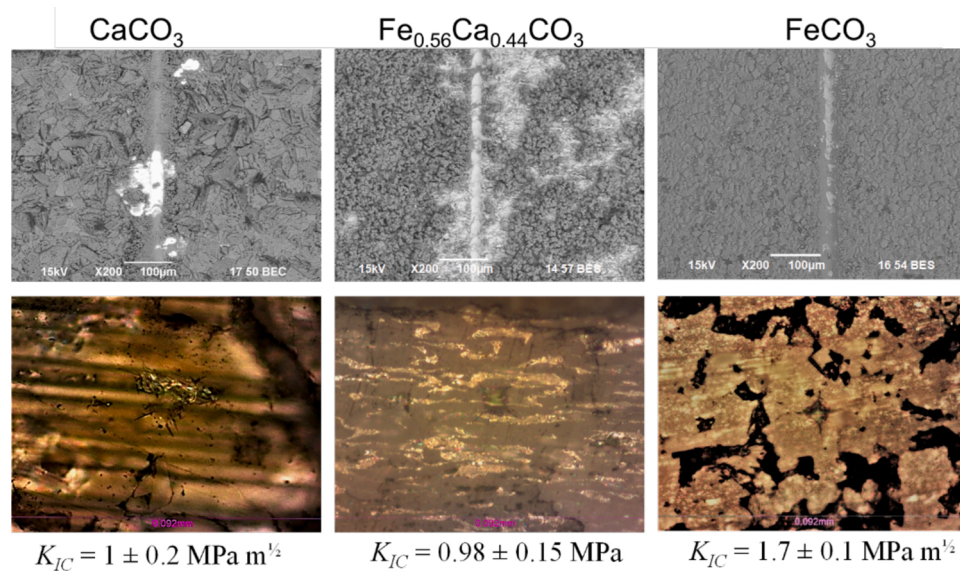


Fig. 22. Vickers hardness mark and crack propagation on a pure calcium carbonate layer, calcium carbonate with substitutional iron atoms, and pure iron carbonate [49]. Scratch direction: from bottom to top.

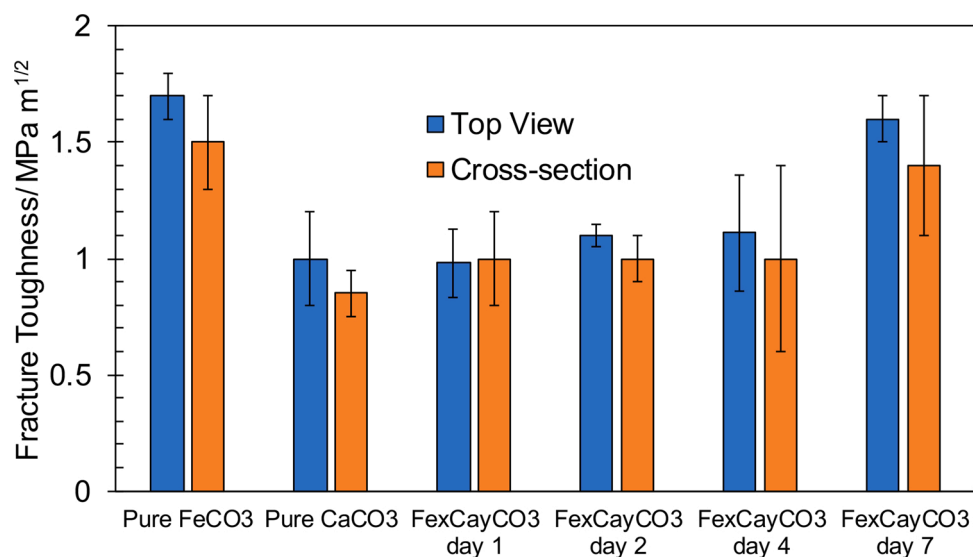


Fig. 23. Summary of fracture toughness (K_{IC}) obtained at the cross-section and the top view of the layers. Error bars: max and minimum values obtained in three different tests.

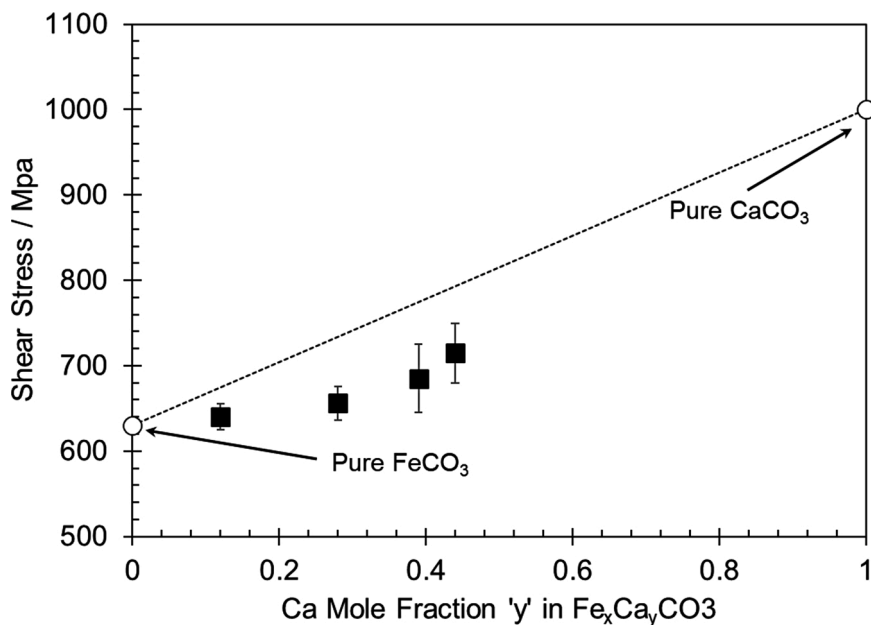


Fig. 24. Critical shear stress to produce an adhesive failure in a $\text{Fe}_x\text{Ca}_y\text{CO}_3$ layer with different Ca mole fraction in the lattice (black squares). Dotted line: linear interpolation between the pure FeCO_3 and CaCO_3 (white circles). Error bars: max and minimum values obtained in three different tests.

mN of the normal force. Finally, the total removal of the layer was found at values in the order of 420 mN, as shown in Fig. 21e. The failures detected and force values are summarized in Table 7.

3.2.2. Vickers Indentation Fracture Tests

Fig. 22 shows the indentation mark and the crack propagation on a calcium carbonate layer with substitutional iron atoms as well as the pure calcium carbonate and pure iron carbonate. The fracture toughness for the iron calcium carbonate layer was determined to be $0.98 \pm 0.15 \text{ MPa m}^{1/2}$, a value close to the pure calcium carbonate ($1 \pm 0.2 \text{ MPa m}^{1/2}$). This result suggests that the fracture toughness of the calcium carbonate layer with substitutional atoms is dominated by the fracture toughness of the pure calcium carbonate.

The summary of the fracture toughness data obtained from the top sides as well as their counterpart cross-sections is shown by Fig. 23. It is observed that the average values between both, cross-section and top, are in good agreement. Therefore, any anisotropic effect can be disregarded.

3.3. Comparison of the Mechanical Integrity of FeCO_3 , CaCO_3 and $\text{Fe}_x\text{Ca}_y\text{CO}_3$ Layers

Fig. 24 shows the comparison of the critical shear stresses to produce an adhesive failure in the layers versus the mole fraction of Ca substituted in the lattice of FeCO_3 . The results demonstrate that the critical shear stress to remove the layers is not a linear function of the

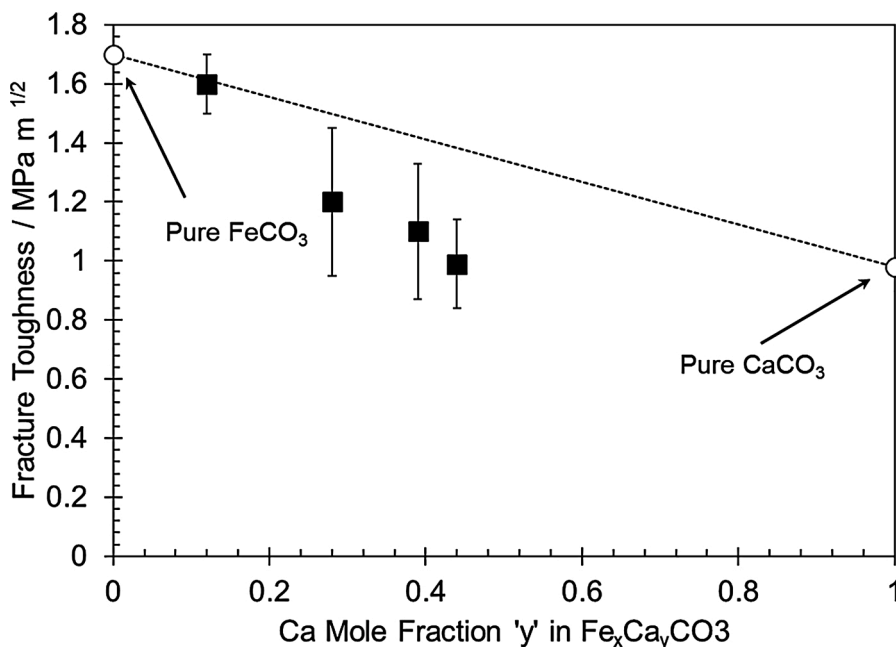


Fig. 25. Fracture toughness values of a $\text{Fe}_x\text{Ca}_y\text{CO}_3$ layer with different Ca mole fraction in the lattice (black squares). Dotted line: linear interpolation between the pure FeCO_3 and CaCO_3 (white circles). Error bars: max and minimum values obtained in three different tests.

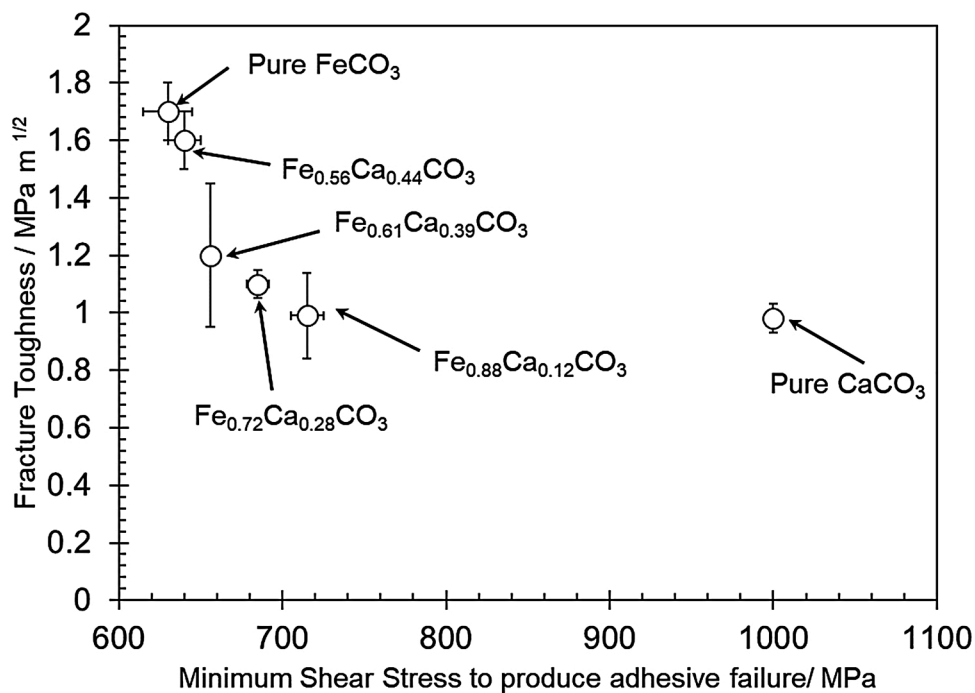


Fig. 26. Plot of fracture toughness *versus* shear stress to produce adhesive failure for different molar composition of the solid solution of $\text{Fe}_x\text{Ca}_y\text{CO}_3$. Vertical error bars: maximum and minimum fracture toughness. Horizontal error bars: maximum and minimum shear stress.

substituted Ca in the lattice, as stated by other researchers [13]; the values are relatively close to the pure iron carbonate layer removal shear stress. This suggests that the adherence between the iron and the iron carbonate is playing a governing role in the mechanical strength of the layer. This postulate is consistent with the layer growth mechanism proposed by Mansoori [7]. Since an iron carbonate layer is growing between the steel and the $\text{Fe}_x\text{Ca}_y\text{CO}_3$ substitutional solid solution, the interaction between the steel and the growing iron carbonate layer governs the detachment of the layer.

The values of fracture toughness *versus* the mole fraction of Ca in the

lattice of iron carbonate were also plotted as shown in Fig. 25. It is noted that the estimated fracture toughness was decreasing in step with calcium substitution in the lattice. However, this relationship is not linear. Contrary to the shear stress, the results are closer to the pure calcium carbonate fracture toughness values in systems with mole fractions of 0.28 Ca or more. This result can be explained by the mechanism of combined corrosion product and scale formation proposed by Mansoori [7]. In his work, the author stated that the calcium carbonate is displaced towards the aqueous bulk solution due to the growth of an iron carbonate layer underneath. Given the nature of the Vickers fracture

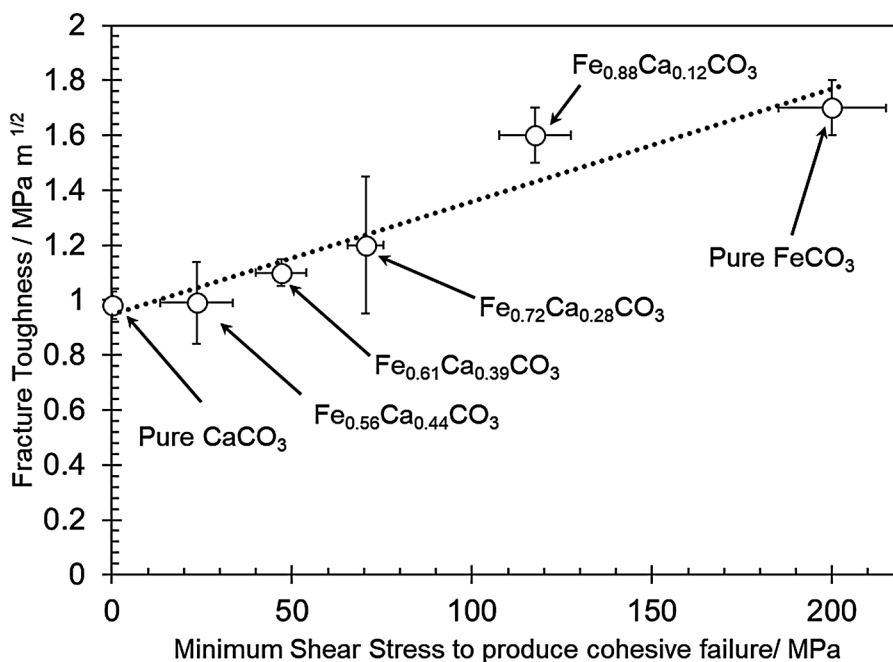


Fig. 27. Correlation between minimum shear stress to produce superficial damage and fracture toughness in the calcium carbonate and iron carbonate layer and with different $\text{Fe}_x\text{Ca}_y\text{CO}_3$ solid solutions. Vertical error bars: maximum and minimum fracture toughness. Horizontal error bars: maximum and minimum shear stress.

toughness measurements, the indentation is performed on the top layer where the composition of calcium is dominant in the carbonate lattice thus explaining the values close to those obtained for pure calcium carbonate.

Fig. 26 shows the plot of fracture toughness values *versus* the shear stress to produce an adhesive failure. There is no linear relationship between the pure iron carbonate and the pure calcium carbonate with solid solution $\text{Fe}_x\text{Ca}_y\text{CO}_3$ layers with different mole fractions of Fe and Ca. Under the assumption that the scratch test measured the forces associated with the adhesion of the layer, this observation suggests that the fracture toughness is not a good indicator of the adhesive properties of the layer. These results are consistent with Quinn [25] that postulated that the Vickers test does not take into consideration all the fracture mechanics involved for a crack propagation, and now it is further demonstrated that this does not provide insights about the adhesive properties of a corrosion product/scale layer.

Nonetheless, Fig. 27 suggests that there exists a correlation between the shear stress associated with cohesive failure and fracture toughness. These values would be related to the bond between the $\text{Fe}_x\text{Ca}_y\text{CO}_3$ and the pure FeCO_3 formed underneath. Since the bond between a layer with structural defects and one with no defects is generally weak [55], the more calcium carbonate at the mentioned interface, the weaker the bonding. Since this layer is placed at the top surface of the specimens, both the scratch test and the Vickers indentation fracture toughness consistently measured the influence of this bonding in relation to the adhesive failure.

Finally, to put all the mechanical integrity data in context, Li, et al. [56], mimicked the conditions encountered in a transportation pipeline and measured the wall shear stress in a single-phase pipe flow and reported values between 10 to 1000 Pa. Therefore, the results obtained in this research indicate that the layers formed in the tested conditions cannot be easily challenged by normal operating conditions of pipelines.

3.4. Corrosion rates

In order to correlate the mechanical integrity of the layers with the protectiveness in terms of corrosion rates, LPR data was taken to determine the instantaneous corrosion rates along with the precipitation

of calcium carbonate and iron calcium carbonate as shown in Fig. 28. As described by Mansoori, et al. [35], there are three corrosion regions during the experiment: active corrosion, nucleation and growth of carbonate layer crystals, and pseudo-passivation. Pseudo-passivation in the context of precipitation of layers refers to the condition of decreasing the corrosion rate and increasing the open circuit potential [35]. Regarding the initial stage (active corrosion) Mansoori [35] reported that the high corrosion rates in the conditions where no calcium was added can be explained by a preferential dissolution of the ferrite phase during the corrosion process. This condition exposes the cementite layer, increasing the cathodic sites for hydrogen evolution [57]. Therefore, a galvanic effect is produced thus accelerating the corrosion process. It can be noted that the active corrosion region in the presence of calcium exhibited lower corrosion rates than its counterpart experiment with no calcium. This result can be explained by the early precipitation of calcium carbonate that avoids the excessive dissolution of ferrite and, therefore, avoiding galvanic coupling effects [35]. For both types of experiment, the corrosion rates started to diminish during the nucleation stage. Mansoori [35] reported that such a diminution is associated with the nucleation and growth of carbonate layers within the cementite exposed during the active corrosion stage.

It can be observed that the corrosion rates in the pseudo-passivation region are similar (after 4 days). This can be attributed to the fact that an iron carbonate layer was formed underneath the initial calcium carbonate layer as reported by Mansoori, et al. [7,35]. Consequently, the presence of calcium carbonate is not detrimental towards the formation of a protective iron carbonate layer despite having different fracture mechanics behavior as suggested by Gao, et al. [11].

4. Conclusions

- The scratch test as applied in this research provides information regarding the mode of failure and provides the parameters required to calculate the critical shear stress, as opposed to indentation tests.
- Regarding the case study, the presence of substitutional calcium in the lattice of iron carbonate was not detrimental in terms of corrosion protection despite having different fracture toughness behavior.

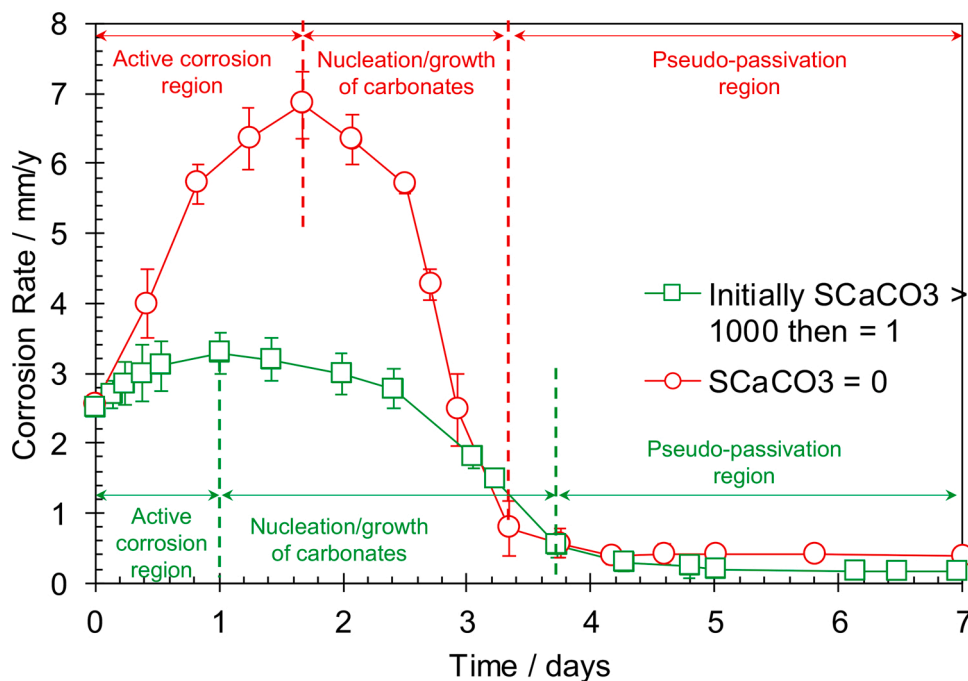


Fig. 28. LPR corrosion rate with time with an initial high saturation of calcium carbonate (green markers) and with no saturation (red markers). Error bars: max and minimum values obtained in three different tests.

Therefore, fragility in terms of fracture toughness of the calcium carbonate cannot be associated with its mechanical removal.

- In terms of mechanical integrity of protective layers, it was demonstrated that the layers could not be easily challenged by the shear stress produced by a transported fluid in pipelines as the values for failure are at least four orders of magnitude higher than the shear stress produced in transporting pipelines.
- One possible cause for failures might be thermal stresses (expansion and contraction of the substrate due to temperature changes). However, this possibility is outwith the scope of this research, but is suggested for future work.

Data Availability

The raw/processed data required to reproduce these findings cannot be shared at the time as the data also forms part of an ongoing study.

CRedit authorship contribution statement

Claudia Prieto: Methodology, Data curation, Writing - original draft, Visualization, Investigation, Validation. **Hamed Mansoori:** Methodology, Investigation. **Bruce Brown:** Validation, Resources, Methodology, Writing - review & editing, Funding acquisition. **Marc Singer:** Conceptualization, Methodology, Resources, Supervision, Writing - review & editing, Funding acquisition. **David Young:** Supervision, Methodology, Writing - review & editing, Project administration.

Declaration of Competing Interest

We have no conflicts of interest to disclose.

Acknowledgments

The authors would like to thank the following companies for their financial support: Anadarko, Baker Hughes, BP, Chevron, CNOOC, ConocoPhillips, DNV GL, ExxonMobil, M-I SWACO (Schlumberger), Multi-Chem (Halliburton), Occidental Oil Company, the Petroleum Institute, PTT, Saudi Aramco, SINOPEC (China Petroleum), and TOTAL.

References

- [1] S. Nešić, A Mechanistic Model for Carbon Dioxide Corrosion of Mild Steel in the Presence of Protective Iron Carbonate Films — Part 2 : A Numerical Experiment, *Corros. Sci.* 59 (2003) 489–497.
- [2] W. Sun, S. Nešić, R.C. Woollam, The effect of temperature and ionic strength on iron carbonate (FeCO₃) solubility limit, *Corros. Sci.* 51 (2009) 1273–1276, <https://doi.org/10.1016/j.corsci.2009.03.009>.
- [3] S. Nešić, K. Lee, A mechanistic model for carbon dioxide corrosion of mild steel in the presence of protective iron carbonate films-Part 3: Film growth model, *Corrosion.* 59 (2003) 616–628.
- [4] W. Sun, Kinetics of Iron Carbonate and Iron Sulfide Scale Formation in CO₂/H₂S Corrosion, Ph.D. Dissertation, Dept. Chem. and Biomolec. Eng., Ohio University, Athens, OH, 2006, https://etd.ohiolink.edu/ap:10.0:::10:P10_ACCESSION_NUM:ohiou1163783193.
- [5] H. Mansoori, D. Young, B. Brown, M. Singer, Influence of calcium and magnesium ions on CO₂ corrosion of carbon steel in oil and gas production systems - A review, *J. Nat. Gas Sci. Eng.* 59 (2018) 287–296, <https://doi.org/10.1016/j.jngse.2018.08.025>.
- [6] S. Nešić, K.L.J. Lee, A mechanistic model for carbon dioxide corrosion of mild steel in the presence of protective iron carbonate films - Part 3: Film growth model, *Corrosion.* 59 (2003) 616–628, <https://doi.org/10.5006/1.3277592>.
- [7] H. Mansoori, D. Young, B. Brown, S. Nešić, M. Singer, Effect of CaCO₃-saturated solution on CO₂ corrosion of mild steel explored in a system with controlled water chemistry and well-defined mass transfer conditions, *Corros. Sci.* 158 (2019) 108078, <https://doi.org/10.1016/j.corsci.2019.07.004>.
- [8] R. Rizzo, S. Gupta, M. Rogowska, R. Ambat, Corrosion of carbon steel under CO₂ conditions: Effect of CaCO₃ precipitation on the stability of the FeCO₃ protective layer, *Corros. Sci.* (2020), <https://doi.org/10.1016/j.corsci.2019.108214>.
- [9] Y. Yang, B. Brown, S. Nešić, M. Elena Gennaro, B. Molinas, Mechanical Strength and Removal of a Protective Iron Carbonate Layer Formed on Mild Steel in CO₂ Corrosion. *NACE Corros. Conf.*, 2010, pp. 1–19.

- [10] G. Schmitt, Fracture mechanical properties of CO₂ corrosion product scales and their relation to localized corrosion. *Corros.* 1996, NACE International, Houston, TX, 1996, pp. 1–21.
- [11] K. Gao, F. Yu, X. Pang, G. Zhang, L. Qiao, W. Chu, M. Lu, Mechanical properties of CO₂ corrosion product scales and their relationship to corrosion rates, *Corros. Sci.* 50 (2008) 2796–2803, <https://doi.org/10.1016/j.corsci.2008.07.016>.
- [12] G. Schmitt, M. Mueller, M. Papenfuss, E. Strobel-Effertz, Understanding localized CO₂ corrosion of carbon steel from physical properties of iron carbonate scales. *NACE Corros. Conf.*, 1999.
- [13] A. Matamoros-Veloz, R. Barker, S. Vargas, A. Neville, Iron Calcium Carbonate Instability: Structural Modification of Siderite Corrosion Films, *ACS Appl. Mater. Interfaces.* (2020), <https://doi.org/10.1021/acsami.0c14513>.
- [14] V. Ruzic, M. Veidt, S. Nešić, Protective iron carbonate films - Part 1: Mechanical removal in single-phase aqueous flow, *Corrosion.* (2006), <https://doi.org/10.5006/1.3278279>.
- [15] V. Ruzic, M. Veidt, S. Nešić, Protective iron carbonate films -Part 2: Chemical removal by dissolution in single-phase aqueous flow, *Corrosion.* (2006), <https://doi.org/10.5006/1.3280674>.
- [16] V. Ruzic, M. Veidt, S. Nešić, Protective iron carbonate films - Part 3: Simultaneous chemo-mechanical removal in single-phase aqueous flow, *Corrosion.* (2007), <https://doi.org/10.5006/1.3278425>.
- [17] L.D. Paolinelli, G.E. Carr, Mechanical integrity of corrosion product films on rotating cylinder specimens, *Corros. Sci.* (2015), <https://doi.org/10.1016/j.corsci.2014.11.042>.
- [18] N.M.M. Ramos, M.L. Simões, J.M.P.Q. Delgado, V.P. De Freitas, Reliability of the pull-off test for in situ evaluation of adhesion strength, *Constr. Build. Mater.* (2012), <https://doi.org/10.1016/j.conbuildmat.2011.12.097>.
- [19] R. Ghavidel, R. Madandoust, M.M. Ranjbar, Reliability of pull-off test for steel fiber reinforced self-compacting concrete, *Meas. J. Int. Meas. Confed.* (2015), <https://doi.org/10.1016/j.measurement.2015.06.013>.
- [20] Y.H. Baek, M.K. Chung, S.M. Son, E.H. Song, C.S. Shin, K.K. Baek, Reliability on coating pull-off adhesion strength test, *NACE - Int. Corros. Conf. Ser.* (2009).
- [21] S.D. Zhu, G.S. Zhou, J. Miao, R. Cai, J.F. Wei, Mechanical Properties of CO₂ Corrosion Scale Formed at Different Temperatures and their Relationship to Corrosion Rate, *Corros. Eng. Sci. Technol.* 47 (2012) 177–181.
- [22] E. Rocha-Rangel, Fracture Toughness Determinations by Means of Indentation Fracture, in: J. Cuppoletti (Ed.), *Nanocomposites with Unique Prop. Appl. Med. Ind.*, 1st ed., Intech, 2011, p. 360.
- [23] H.A. Richard, M. Sander, Fundamentals of fracture mechanics. *Solid Mech. Its Appl.*, 2016, https://doi.org/10.1007/978-3-319-32534-7_3.
- [24] B.R. Lawn, D.B. Marshall, Hardness, toughness, and brittleness: an indentation analysis, *J. Am. Ceram. Soc.* 62 (1978) 347–350.
- [25] G.D. Quinn, R.C. Bradt, On the vickers indentation fracture toughness Test, *J. Am. Ceram. Soc.* (2007) 673–680, <https://doi.org/10.1111/j.1551-2916.2006.01482.x>.
- [26] D. Chicot, G. Duarte, A. Tricoteaux, B. Jorgowski, A. Leriche, J. Lesage, Vickers Indentation Fracture (VIF) modeling to analyze multi-cracking toughness of titania, alumina and zirconia plasma sprayed coatings, *Mater. Sci. Eng. A.* 527 (2009) 65–76, <https://doi.org/10.1016/j.msea.2009.08.058>.
- [27] C. Weaver, Adhesion of thin films, *J. Vac. Sci. Technol.* 12 (1975) 18–25, <https://doi.org/10.1116/1.568754>.
- [28] S.J. Bull, D.S. Rickerby, A. Matthews, A. Leyland, A.R. Pace, J. Valli, The use of scratch adhesion testing for the determination of interfacial adhesion: The importance of frictional drag, *Surf. Coatings Technol.* 36 (1988) 503–517, [https://doi.org/10.1016/0257-8972\(88\)90178-8](https://doi.org/10.1016/0257-8972(88)90178-8).
- [29] S.J. Bull, E.G. Berasategui, An overview of the potential of quantitative coating adhesion measurements by scratch testing, *Tribol. Int.* 39 (2006) 136–165, <https://doi.org/10.1016/j.triboint.2005.04.013>.
- [30] S.J. Bull, D.S. Rickerby, New developments in the modelling of the hardness and scratch adhesion of thin films, *Surf. Coatings Technol.* 42 (1990) 149–164, [https://doi.org/10.1016/0257-8972\(90\)90121-R](https://doi.org/10.1016/0257-8972(90)90121-R).
- [31] A.J. Perry, The adhesion of chemically vapour-deposited hard coatings to steel-the scratch test, *Thin Solid Films.* 78 (1981) 77–94, [https://doi.org/10.1016/0040-6090\(81\)90419-3](https://doi.org/10.1016/0040-6090(81)90419-3).
- [32] P. Benjamin, C. Weaver, Measurement of adhesion of thin films, *Proc. R. Soc. London. Ser. A. Math. Phys. Sci.* 254 (1960) 163–176, <https://doi.org/10.1098/rspa.1960.0012>.
- [33] M.T. Laugier, Adhesion of TiC and TiN coatings prepared by chemical vapour deposition on WC-Co-based cemented carbides, *J. Mater. Sci.* 21 (1986) 2269–2272, <https://doi.org/10.1007/BF01142666>.
- [34] B. Ollivier, A. Matthews, Adhesion of diamond-like carbon films on polymers: an assessment of the validity of the scratch test technique applied to flexible substrates, *J. Adhes. Sci. Technol.* 8 (1994) 651–662, <https://doi.org/10.1163/156856194X00401>.
- [35] H. Mansoori, B. Brown, D. Young, S. Nešić, M. Singer, Effect of Fe_xCa_yCO₃ and CaCO₃ scales on the CO₂ corrosion of mild steel, *Corrosion.* (2019), <https://doi.org/10.5006/3290>.
- [36] S. Nešić, Key issues related to modelling of internal corrosion of oil and gas pipelines – A review, *Corros. Sci.* 49 (2007) 4308–4338, <https://doi.org/10.1016/j.corsci.2007.06.006>.
- [37] M. Dietzel, Carbonates, in: J. Reitner, V. Thiel (Eds.), *Encycl. Geobiol.*, Springer Netherlands, Dordrecht, 2011, pp. 261–266, https://doi.org/10.1007/978-1-4020-9212-1_50.
- [38] N. Spanos, P.G. Koutsoukos, Kinetics of precipitation of calcium carbonate in alkaline pH at constant supersaturation. Spontaneous and seeded growth, *J. Phys. Chem. B.* (1998), <https://doi.org/10.1021/jp981171h>.

- [39] ASTM, ASTM G102 - 89(2010) Standard Practice for Calculation of Corrosion Rates and Related Information from Electrochemical Measurements. Annu. B. ASTM Stand., 2010.
- [40] E. McCafferty, Introduction to Corrosion Science, 2010, <https://doi.org/10.1017/CBO9781107415324.004>.
- [41] V. Fajardo, C. Canto, B. Brown, D. Young, S. Nescic, The effect of acetic acid on the integrity of protective iron carbonate layers in CO₂ corrosion of mild steel. NACE Corros. Conf., NACE International, Houston, TX, 2008.
- [42] E. Gulbrandsen, Acetic acid and carbon dioxide corrosion of carbon steel covered with iron carbonate. NACE Corros. Conf., 2007.
- [43] S.J. Bull, Failure mode maps in the thin film scratch adhesion test, Tribol. Int. 30 (1997) 491–498.
- [44] D. Dowson, C.M. Taylor, T.H.C. Childs, M. Godet, Thin Films in Tribology, Elsevier, London, 1993.
- [45] B. Lafuente, R.T. Downs, H. Yang, N. Stone, in: T. Armbruster, R.M. Danisi (Eds.), RRUFF™ Project, Power Databases RRUFF Proj. Highlights Mineral. Crystallogr., 2015.
- [46] Y. Hua, A. Shamsa, R. Barker, A. Neville, Protectiveness, morphology and composition of corrosion products formed on carbon steel in the presence of Cl⁻, Ca²⁺ and Mg²⁺ in high pressure CO₂ environments, Appl. Surf. Sci. (2018), <https://doi.org/10.1016/j.apsusc.2018.05.140>.
- [47] D. Brandon, W.D. Kaplan, Microstructural Characterization of Materials, 2nd Edition, 2008, <https://doi.org/10.1002/9780470727133>.
- [48] ASTM, Standard Test Method for Adhesion Strength and Mechanical Failure Modes of Ceramic Coatings by Quantitative Single Point Scratch Testing, ASTM Int. C1624-05, 2010, pp. 1–29, <https://doi.org/10.1520/C1624-05R10.Scope>.
- [49] C. Prieto, E. Anyanwu, D. Young, M. Singer, Mechanical Characterization and Adherence of Iron Carbonate on an X65 Steel, Corrosion (2019) 1–15.
- [50] X. Yin, J. Shi, X. Niu, H. Huang, X. Wang, Wedding Cake Growth Mechanism in One-Dimensional and Two-Dimensional Nanostructure Evolution, Nano Lett. (2015), <https://doi.org/10.1021/acs.nanolett.5b04072>.
- [51] M. Wen, H. Huang, K. Zhang, Q. Meng, X. Li, L. Kong, C. Hu, W. Zheng, The AlN layer thickness dependent coherent epitaxial growth, stress and hardness in NbN/AlN nanostructured multilayer films, Surf. Coatings Technol. (2013), <https://doi.org/10.1016/j.surfcoat.2013.08.004>.
- [52] J.A. Floro, E. Chason, R.C. Cammarata, D.J. Srolovitz, Physical origins of intrinsic stresses in Volmer-Weber thin films, MRS Bull. (2002), <https://doi.org/10.1557/mrs2002.15>.
- [53] S. Pandya, A.R. Damodaran, R. Xu, S.L. Hsu, J.C. Agar, L.W. Martin, Strain-induced growth instability and nanoscale surface patterning in perovskite thin films, Sci. Rep. (2016), <https://doi.org/10.1038/srep26075>.
- [54] J.L. Beuth, Cracking of thin bonded films in residual tension, Int. J. Solids Struct. 29 (1992) 1657–1675, [https://doi.org/10.1016/0020-7683\(92\)90015-L](https://doi.org/10.1016/0020-7683(92)90015-L).
- [55] B. Bushan, Handbook of Micro/Nanotribology, 1st Editio, CRC Press LLC, Boca Raton, FL, 1999.
- [56] W. Li, B.F.M. Pots, B. Brown, K.E. Kee, S. Nescic, A direct measurement of wall shear stress in multiphase flow-Is it an important parameter in CO₂ corrosion of carbon steel pipelines? Corros. Sci. 110 (2016) 35–45, <https://doi.org/10.1016/j.corsci.2016.04.008>.
- [57] J.L. Crolet, N. Thevenot, S. Nescic, Role of Conductive Corrosion Products in the Protectiveness of Corrosion Layers, Corrosion. (1998), <https://doi.org/10.5006/1.3284844>.